

Article

Devitrification Behavior of Sol-Gel Derived $\text{ZrO}_2\text{-SiO}_2$ Rare-Earth Doped Glasses: Correlation between Structural and Optical Properties

Masato Isogai ^{1,†}, Alexander Veber ^{2,†,*} , Maria Rita Cicconi ², Tomokatsu Hayakawa ¹ and Dominique de Ligny ²

¹ Department of Frontier Materials, Graduate School of Engineering, Nagoya Institute of Technology, Gokiso, Showa, Nagoya, Aichi 466-8555, Japan; 29411020@stn.nitech.ac.jp (M.I.); hayatomo@nitech.ac.jp (T.H.)

² Institute of Glass and Ceramics, Department of Materials Science and Engineering, University of Erlangen-Nuremberg, Martensstraße 5, DE-91058 Erlangen, Germany; maria.rita.cicconi@fau.de (M.R.C.); dominique.de.ligny@fau.de (D.L.)

* Correspondence: alexander.veber@fau.de; Tel.: +49-9131-85-20378

† Both authors contributed equally to this manuscript

Received: 13 September 2018; Accepted: 2 October 2018; Published: 7 October 2018



Abstract: Optical and structural properties of glasses and glass-ceramics (GC) obtained by different heat-treatment of Tb and Tb-Yb doped sol-gel derived $30\text{ZrO}_2\text{-}70\text{SiO}_2$ materials were investigated. A glass was formed after treatment at $700\text{ }^\circ\text{C}$ whereas devitrification of the media after the treatment at 1000 and $1100\text{ }^\circ\text{C}$, led to the formation of GC containing up to three different crystalline phases, namely, tetragonal ZrO_2 , Yb-disilicate and cristobalite. The modification of the optical properties through the heat treatment was caused by redistribution of the rare earth elements (REE) among the different phases: both Tb and Yb entered the t- ZrO_2 lattice, Yb can also be present in the form of a $\text{Yb}_2\text{Si}_2\text{O}_7$ crystal. Devitrification led to an increase in Tb→Yb energy transfer efficiency as compared to the glass, though it was higher in the samples heat-treated at $1000\text{ }^\circ\text{C}$ than in those treated at $1100\text{ }^\circ\text{C}$. The most intensive Yb^{3+} luminescence, induced by the energy transfer from the Tb^{3+} ion, was observed at the interface between t- ZrO_2 and the glassy phases, due to the high concentration of REE in this area caused by the inability of ZrO_2 to accept larger amounts of the REE. The mechanisms of the Tb→Yb energy transfer vary between different phases of the GC. The results obtained in this study are important for the development of spectral down-converters for potential solar energy applications based on Tb-Yb co-doped glass-ceramics.

Keywords: down-conversion; solar cells; glass; glass ceramics; devitrification; sol-gel; rare-earth

1. Introduction

Development of alternative environmentally friendly energy sources is an important issue today. Use of solar panels for electricity generation appears to be one of the most promising solutions. Owing to advanced development of silicon technologies, relatively low-cost Si solar cells are currently the most widely used. However conversion efficiency is limited to $\sim 30\%$ due to spectral mismatch [1]. This value can be increased by conversion of the UV and IR light coming from the Sun into a light range more suitable for these solar cells. Infrared photons can be converted into more energetic ones using up-conversion [2,3]. Higher energy photons can be transformed into the optimal absorption region using down-shifting or down-conversion (also known as quantum cutting) processes. The latter mechanism is preferable, since it implies conversion of one high energy photon into two photons of optimal energies, resulting in a theoretical quantum efficiency of 200%.

Down-conversion can be realized using a pair of REE [3]. Here, the Yb^{3+} ion serves as a perfect acceptor ion, since its emission is well matched with the c-Si solar cell energy gap. Moreover, issues associated with excited-state absorption, up-conversion and concentration quenching can be eliminated due to the presence of only one excited 4f manifold in the ion, allowing the use of high doping concentrations. Down-conversion was demonstrated for different REE- Yb^{3+} pairs in [2] and references therein, where REE can be Ce^{3+} , Pr^{3+} , Eu^{3+} , Ho^{3+} , Tm^{3+} , and Tb^{3+} . Also, it was shown that quantum cutting can be obtained in Tb-Yb co-doped materials [4–7]. The quantum efficiency of the cooperative energy transfer from single Tb^{3+} to two Yb^{3+} ions observed experimentally can be as high as 196% [8].

Choice of the host material is a very important parameter for the potential practical applications. Sol-gel derived ZrO_2 - SiO_2 glasses are a good candidate in this case; lower phonon energies as compared to pure SiO_2 glass can lead to higher quantum efficiency (QE) of the REE emission, and use of the sol-gel process allows the acquisition of a variety of chemical compositions with up to 50 mol. % ZrO_2 [9], which is not possible using classic high temperature melt techniques. These glasses possess good corrosion resistance and a low thermal expansion coefficient, which are important for outdoor applications. As an additional benefit these glasses can be easily crystallized under heat treatment, forming glass ceramics with embedded ZrO_2 crystals. Visible to near-infrared (NIR) down-conversion has been demonstrated for Tb and Yb doped nanocrystalline ZrO_2 [10]. Thus, devitrification of the glasses could lead to more luminescence efficient GC materials since emission QE of crystalline materials is typically higher, as has been successfully demonstrated for silica-hafnia glass ceramics [5,11] or Eu doped aluminosilicate glasses [12]. Metal-silicate systems, where the metal can be Zr, Hf, Y or La, deserve special attention here since these materials are particularly suitable for decomposition into a metal- and silica-rich phases in a quite broad range of SiO_2 content [13], which affects the crystallization behavior [14]. Moreover, HfO_2 - SiO_2 system and ZrO_2 - SiO_2 system phase diagrams are very similar [15,16], having the middle of their miscibility gap at approximately 30 mol. % of the metal oxide content [13]. Therefore it can be expected, that 30 ZrO_2 -70 SiO_2 based materials will obtain GC materials with optical performances similar to previously demonstrated 30 HfO_2 -70 SiO_2 based glass ceramics [5,11].

2. Materials and Methods

In the present study 30 ZrO_2 -70 SiO_2 glasses and glass ceramic materials doped solely with 1 mol % Tb_2O_3 or with 1 mol % Tb_2O_3 and 10 mol. % Yb_2O_3 were investigated. First, the gels were synthesized following a standard procedure described in [9,14,17], using zirconium(IV) isopropoxide, tetraethyl orthosilicate, and terbium and ytterbium chloride hexahydrate as the raw components. Then, the gels were heat treated at different temperatures for different periods of time: 700 °C for 7 h, and at 1000 and 1100 °C for 2, 5, 10 and 30 hours for both the temperatures. The bulk samples with an approximate size of 5 mm × 5 mm × 1 mm were obtained after the treatment. The notation “T/t”, where “T” and “t” are temperature and time of the heat-treatment is used within the manuscript, e.g., 700/7 is used for the sample treated at 700 °C for 7 hours. The doping is identified within the text with additional suffixes: Tb and Tb-Yb are referred to as Tb-only and Tb-Yb co-doped samples, respectively.

Fluorescence spectroscopy characterization was performed using a UV-Vis-NIR fluorometer equipped with TSCPS system (Fluorolog 3, Horiba Scientific, Edison, NJ, USA) with 450 W CW and 70 W pulsed Xe-lamps as the excitation source for steady state and time-resolved experiments, respectively. Time response of the experimental setup was limited by the lamp (~1 μs).

Structural characterization of the samples was performed using Raman spectroscopy, which distinguishes different ZrO_2 phases more easily compared to X-Ray diffraction (XRD). Raman mapping was performed using a Raman microscope (Nicolet Almega XR, Thermo Fischer Scientific, Waltham, MA, USA). Under the excitation with a 532 nm laser, the Raman signal does not interfere with the luminescence of the REE. Additional XRD characterization was done for Tb-Yb co-doped 1100 °C treated samples using the Kristalloflex D500 system (Siemens AG, Karlsruhe, Germany).

In this study, the Raman microscope was also used as a confocal fluorescence microscope. The Almaga XR Raman microscope with a 780 nm laser was used as an excitation source to directly map excited Yb^{3+} luminescence whereas a modular Raman-spectrometer based on a monochromator (iHR 320, Horiba Scientific, Edison, NJ, USA), 488 nm laser (Sapphire SF 488, Coherent, CA, USA) and equipped with an XY-stage (based on the ARABICA experimental setup, described in detail in [18]) was used for micro characterization of directly excited Tb^{3+} emission and indirectly excited Yb^{3+} luminescence. All maps obtained on the different equipment have a similar lateral spatial resolution of about 1 μm .

3. Results and Discussion

All the samples possessed the NIR luminescence emitted by Yb^{3+} under the direct excitation of this ion with $\lambda_{\text{ex}} = 920 \text{ nm}$ (Figure 1a). The higher the temperature and the longer the time of the treatment, the greater the observed changes in Yb^{3+} luminescence as compared to 700/7 *Tb-Yb* sample. Additional sharp bands appeared at 955, 965 and 1035–1038 nm whereas the main band shifted from 976 to 974 nm. These changes were the greatest in the samples treated at 1100 °C for 10 and 30 h. It showed that Yb^{3+} occupied additional sites with different environments. For all the samples, $\text{Tb} \rightarrow \text{Yb}$ energy transfer was observed and the Yb^{3+} NIR luminescence was detected under 488 nm excitation (Figure 1b). The luminescence spectra observed in this case were found to be similar to the directly excited ($\lambda_{\text{ex}} = 920 \text{ nm}$). As one can see in Figure 1a,b, only between 700/7 samples the spectra differ significantly with change of the excitation wavelength. The noticeable difference between direct and indirect excitation emission spectra are due to the lower spectrometer resolution used with excitation at 488 nm.

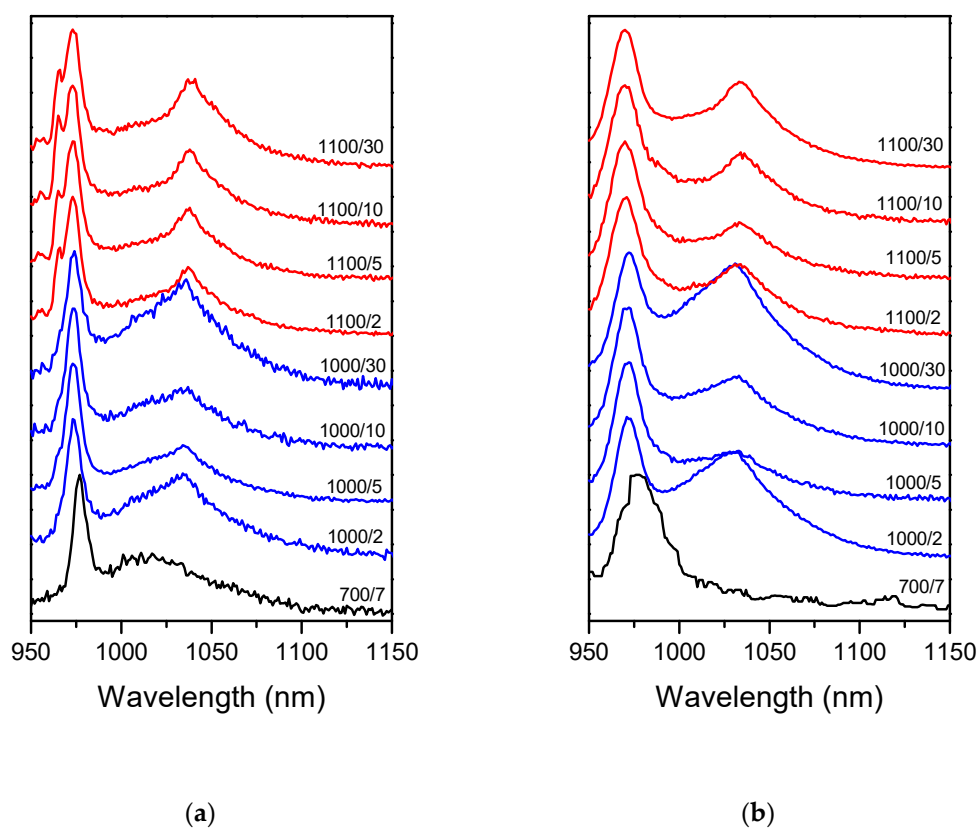


Figure 1. Emission spectra of Yb^{3+} ($^5\text{F}_{5/2} \rightarrow ^2\text{F}_{7/2}$) obtained for the samples after different heat treatment when the ion was excited directly with $\lambda_{\text{ex}} = 920 \text{ nm}$ (a); due to the $\text{Tb} \rightarrow \text{Yb}$ energy transfer with $\lambda_{\text{ex}} = 488 \text{ nm}$ (b). In the latter case, the spectra were recorded with a lower spectral resolution. Temperature and time of the treatment are shown in the plots on the right side of each spectrum.

The samples obtained possessed visible luminescence originating from the Tb^{3+} ion. As was shown before for Yb^{3+} emission, Tb^{3+} spectra also evolve with treatment temperature and time (Figure 2a and 2b for Tb and Tb-Yb doped samples, respectively). At least two Stark sub-components became visible for $^5D_4 \rightarrow ^7F_5$ and $^5D_4 \rightarrow ^7F_4$ transitions after the treatment at 1000 and 1100 °C, evidencing formation of new Tb^{3+} sites with different strength and symmetry of the crystal field around the ions. Moreover, small differences could be seen between Tb (Figure 2a) and Tb-Yb doped (Figure 2b) samples treated at 1100 °C. In the case of Tb-Yb samples, the emission spectra were more resolved and after 30 hours, three components were clearly visible for $^5D_4 \rightarrow ^7F_5$ transition whereas only two could be distinguished with the naked eye for the Tb-only doped sample. Thus, even with the same thermal history of the samples, co-doping with Yb^{3+} influenced Tb^{3+} environment.

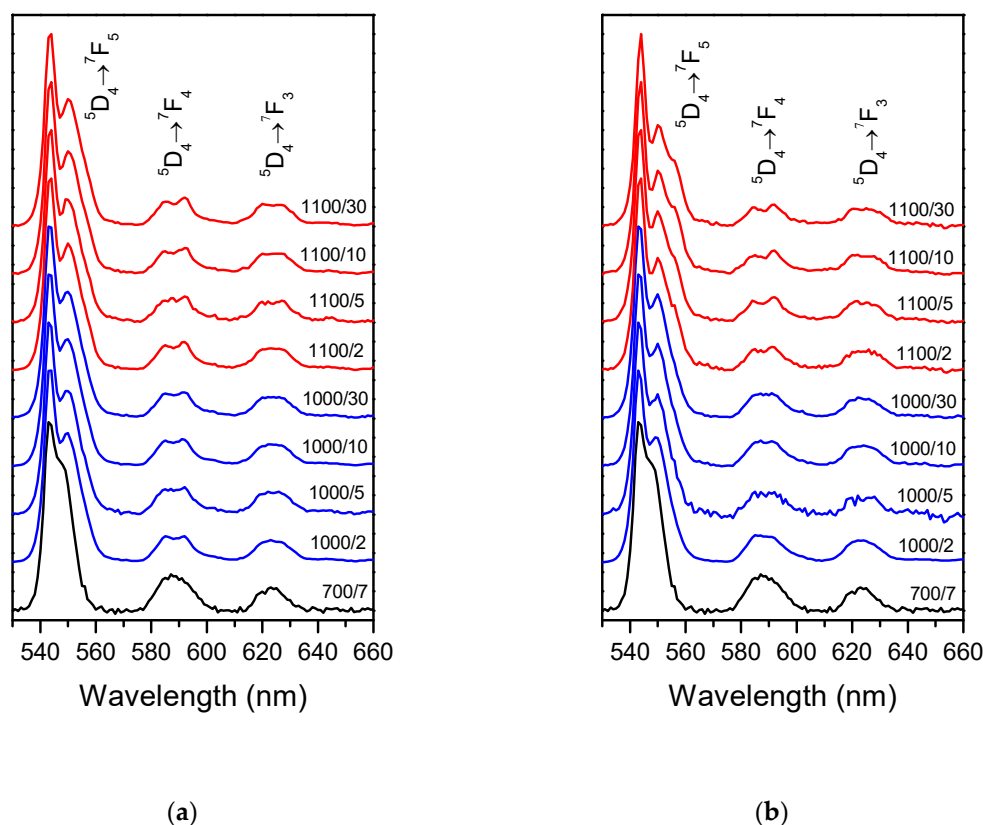


Figure 2. Emission spectra of Tb^{3+} obtained for Tb-doped (a) and Tb-Yb-doped (b) samples after different heat treatment, $\lambda_{ex} = 488$ nm. Temperature and time of the treatment are given in the plots on the right side of each spectrum.

Luminescence decay curves recorded under excitation at 488 nm and emission at 542 nm are found to be mono-exponential for all Tb-only doped samples (Figure 3a,b) and strongly non-exponential for Tb-Yb doped samples (Figure 3c,d). Using these experimental data, the effective luminescence time was calculated as $\tau_{eff} = \int I(t) \cdot t \cdot dt / \int I(t) \cdot dt$ [19]. The effective lifetimes obtained are shown in the insets of Figure 3a–d. For 700/7 samples (not shown in Figure 3) the lifetimes were 2.63 and 2.15 ms for Tb-only and Tb-Yb doped samples, respectively. For Tb-only doped samples Tb^{3+} lifetime barely changed with the heat treatment and remained around 2.7 ms. On co-doping with Yb, the decay curves became non-exponential and effective lifetimes decreased significantly in Tb-Yb as compared to Tb-doped samples. This evidences the existence of Tb→Yb energy transfer. For the samples obtained at 1000 °C, the effective lifetime of Yb-Tb samples decreased with the treatment time. This was not the case for the samples treated at 1100 °C, the lifetime of which slightly increased after 30 hours as compared to 2 hours of treatment.

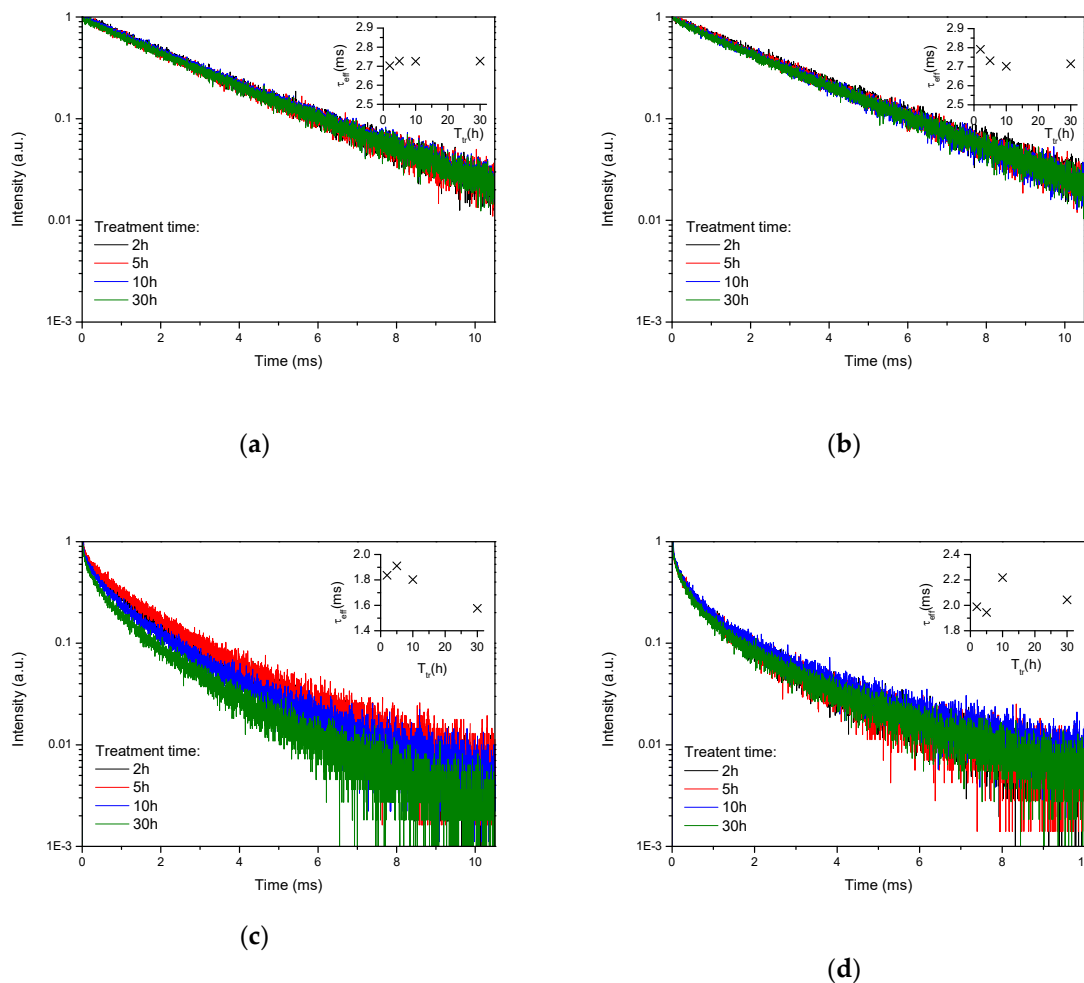


Figure 3. Luminescence decay curves recorded under excitation at 488 nm and emission at 542 nm for (a) Tb-doped samples treated at 1000 °C; (b) Tb-doped samples treated at 1100 °C; (c) Tb-Yb-doped samples treated at 1000 °C, and (d) Tb-Yb-doped samples treated at 1100 °C. The calculated effective times are shown in the insets.

The values of the effective lifetime, τ_{eff} , were used to estimate the energy transfer efficiency (ETE) as $\eta_{\text{ETE}} = 1 - \tau_{\text{TbYb}} / \tau_{\text{Tb}}$ [4], the result is shown in Figure 4. An energy transfer with efficiency of about 18% was already observed in 700/7 Tb-Yb sample. The heat treatment at higher temperatures for 2 hours increased this value up to around 30%. Longer treatment further advanced this parameter in the case of 1000 °C samples up to 42% after 30 hours, whereas stagnation or even a small decrease was observed for 1100 °C samples.

The structural changes induced by the heat treatment were studied to try to correlate them with the observed changes in optical properties. The Raman spectra of 700/7 samples had no sharp peaks (Figure 5) and agrees well with the literature spectrum of undoped $\text{ZrO}_2\text{-SiO}_2$ sol-gel derived glass of similar composition [20]. After the heat treatment at higher temperatures, the spectra of Tb-only samples were dominated by sharp peaks (Figure 5). According to the literature, these vibrational bands were assigned to tetragonal ZrO_2 phase [21–24]. This means that the crystallinity of Tb-only doped samples increases with time and temperature. The same trend was observed for Tb-Yb samples during the 1000 °C treatment. However, at 1100 °C the spectra look more amorphous than crystalline (Figure 5).

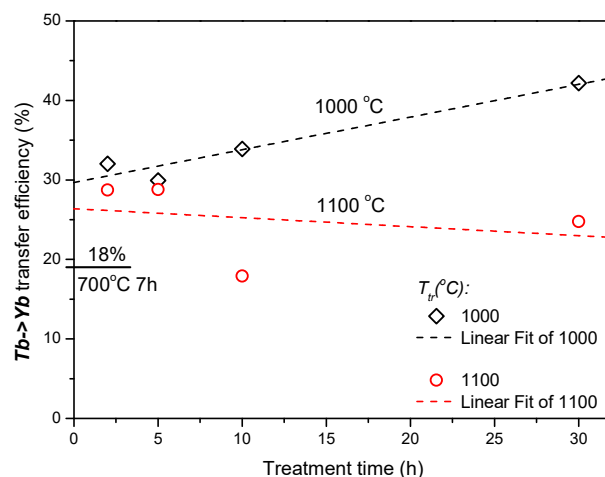


Figure 4. The Tb→Yb energy transfer efficiency for different heat treatment periods and temperatures.

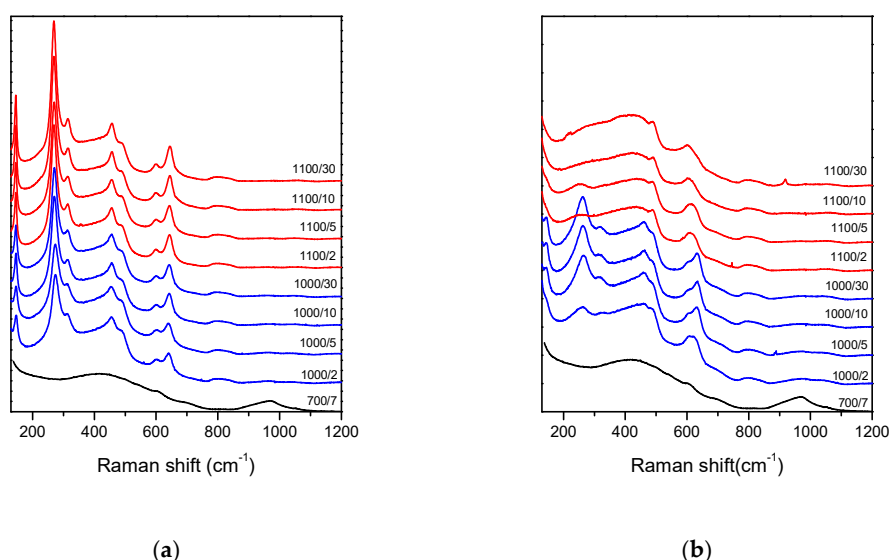


Figure 5. Raman scattering spectra of (a) Tb-only and (b) Tb-Yb samples after different heat treatment. The spectra were recorded under 532 nm laser excitation. Temperature and time of the treatment are given in the plots on the right side of each spectrum.

Additional XRD analysis was done for this series of the samples, which confirmed an increase of the crystallinity with an increase in the heat treatment time (Figure 6). With the XRD analysis it is hard to distinguish whether the diffraction peaks originate from the tetragonal or cubic ZrO₂ phase [25], however, further analysis of the samples by means of Raman spectroscopy (see below), confirmed the presence of the t-ZrO₂ phase.

According to the literature data, an undoped 30ZrO₂-70SiO₂ sol-gel system at treatment temperatures below 1200 °C should stabilize in the tetragonal phase [26]. Doping with REE can shift the equilibrium and lead to stabilization of different ZrO₂ polymorphs [27], but according to our results this is not the case for the sol-gel derived samples analyzed in this study.

The Raman spectra of 1100 °C Tb-Yb samples were found to vary from point to point, presenting big spatial inhomogeneities (Figure 7). It is important to mention that this effect was not observed for Tb-only doped samples and 1000 °C Tb-Yb samples, and these materials can be considered to be homogeneous within a micrometric scale. The detected samples inhomogeneity was investigated in more detail for 1100/30 Tb-Yb sample. It was found that crystalline inclusions with sizes of up to 30 μm

were formed in 1100/30 *Tb-Yb* sample (Figure 8a). These rather large crystalline inclusions look mostly monocrystalline. They are surrounded by apparent cracks disposed radially. These cracks probably appeared due to the mismatch in thermal expansion coefficients of the different phases.

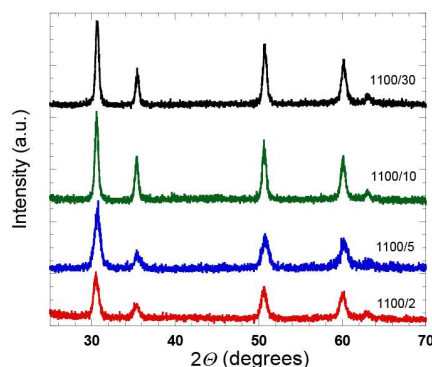


Figure 6. X-ray diffraction pattern of the *Tb-Yb* doped samples heat treated at 1100 °C.

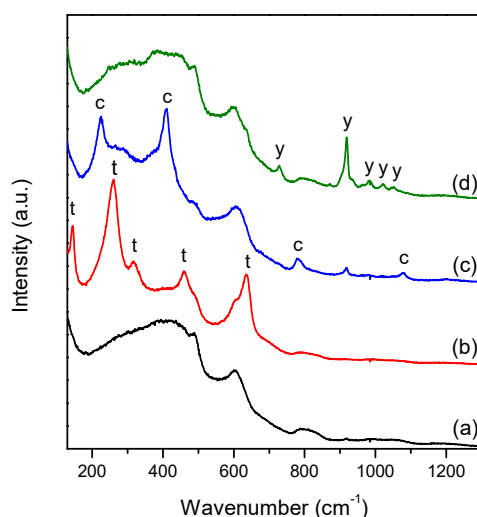


Figure 7. Selected spectra observed with the Raman spectroscopy ($\lambda_{\text{ex}} = 532 \text{ nm}$) in different points of 1100/30 *Tb-Yb* sample. The observed phases in the spectra are (a) glass phase; (b) tetragonal ZrO_2 ; (c) cristobalite; and (d) $\text{Yb}_2\text{Si}_2\text{O}_7$. All the spectra represent a superposition of bands originating from all the phases. Characteristic vibrational lines correspondent to a specific phase are marked in each plot.

Point by point Raman mapping was done for the area close to one of such crystalline inclusions. The structural properties of this can be described by the presence of 4 different phases: glassy phase, tetragonal ZrO_2 , SiO_2 cristobalite and $\text{Yb}_2\text{Si}_2\text{O}_7$. Their characteristic Raman spectra are shown in Figure 7, curves a-d, respectively. The *Yb*-disilicate has different polymorphs. According to previous studies, the stabilized polymorph depends on the REE ionic radius and for Yb^{3+} , the β phase of the crystal should be the most favorable [28]. Nevertheless, the Raman spectrum observed in our study does not match the literature data [29], but it was found to be very similar to $\delta\text{-Y}_2\text{Si}_2\text{O}_7$ [30]. This could be evidence that $\delta\text{-Yb}_2\text{Si}_2\text{O}_7$ phase was stabilized in our case.

The spectrum of the amorphous phase in 1100/30 *Tb-Yb* differs significantly from the one in 700/7 *Tb-Yb*. After the heat treatment, the residual amorphous phase looks to be closer to the silica glass spectrum [31]. This is reasonable, since part of REE and Zr left the glass to form novel crystalline phases.

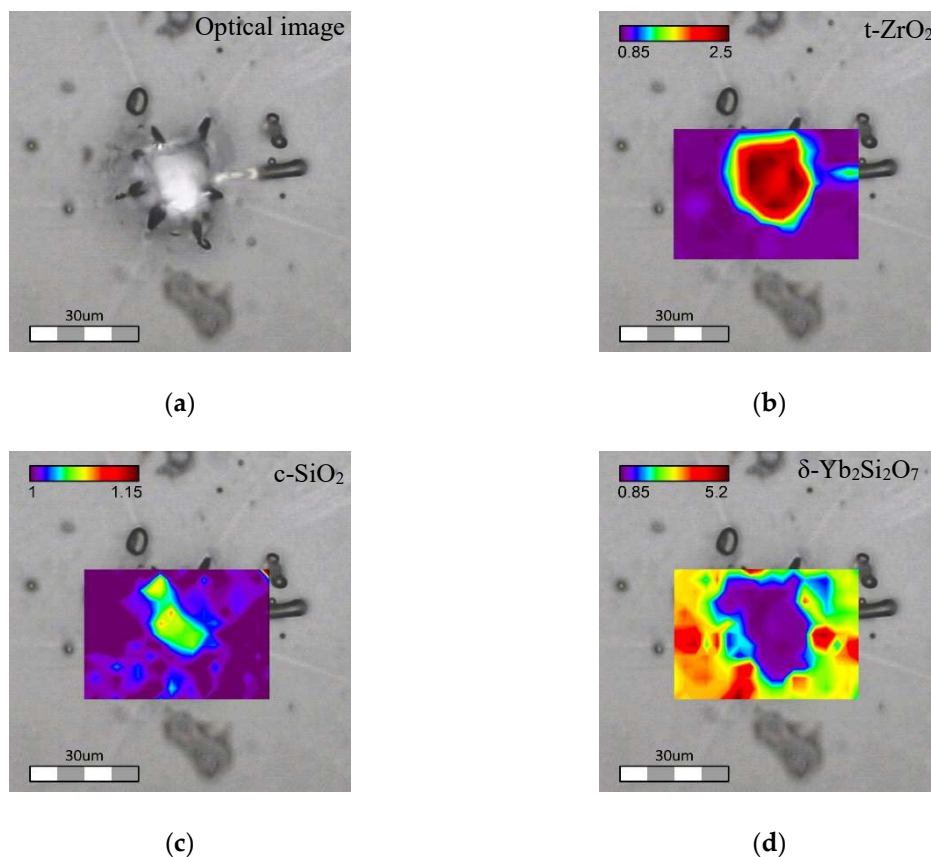


Figure 8. Results of detailed investigation of 1100/30 Tb-Yb sample using Raman microspectrometer ($\lambda_{\text{ex}} = 532 \text{ nm}$): the microscopic image of the investigated area (a); distribution of tetragonal ZrO_2 (b) SiO_2 cristobalite (c) and $\text{Yb}_2\text{Si}_2\text{O}_7$ (d) phases. A rainbow palette was used for all the plots—violet and red colors correspond to the lowest and the highest value of the calculated ratios/phase amount respectively.

To estimate the number of different phases over the investigated area, for each crystalline phase two spectral points were chosen: one corresponding to a characteristic vibrational band and the second was taken close to the first, but where only the glassy phase had a contribution. After, the relative intensity between these two peaks was calculated to get an appropriate Raman image. Thus, distribution of the crystalline phases was estimated by calculating the relative intensity of characteristic peaks: intensities at 410 cm^{-1} over 378 cm^{-1} for cristobalite, 260 cm^{-1} over 369 cm^{-1} for t- ZrO_2 and 919 cm^{-1} over 887 cm^{-1} for $\text{Yb}_2\text{Si}_2\text{O}_7$ crystalline phases. The results of these recalculations are shown in Figure 8b–d.

As one can see on the phase distribution maps (Figure 8), the big crystalline inclusions are formed by t- ZrO_2 . Excess of “free” SiO_2 after crystallization of the pure zirconium crystal results in formation of cristobalite phase located mostly at the same area as t- ZrO_2 . Since the t- ZrO_2 seems transparent and monocrystalline in the optical image, the cristobalite presence needs to be imagined as small local crystalline phases embedded in the t- ZrO_2 crystal itself. Ytterbium disilicate, having some concentrated spots, was detected almost everywhere except the t- ZrO_2 area. As can be seen in Figure 8d, the location of $\text{Yb}_2\text{Si}_2\text{O}_7$ seems to be correlated with the presence of the radial cracks.

Point by point luminescence mapping of the area around the same crystal was done using Raman confocal microscopes under excitation at 488 and 780 nm. The blue and the infrared lasers directly excited Tb^{3+} and Yb^{3+} ions, respectively, and their emission spectra were recorded. Moreover, Yb^{3+} luminescence excited through the energy transfer from Tb^{3+} ion was collected under 488 nm excitation.

The luminescence spectra collected were analyzed for two aspects: integral intensity of the emission (Figure 9a,c,f for $\text{Tb}^{3+}/\lambda_{\text{ex}} = 488 \text{ nm}$, $\text{Yb}^{3+}/\lambda_{\text{ex}} = 780 \text{ nm}$ and $\text{Yb}^{3+}/\lambda_{\text{ex}} = 488 \text{ nm}$ emission, respectively) and change in relative intensities between different emission components. In the case of the Tb^{3+} ratio between subcomponents of $^5\text{D}_4 \rightarrow ^7\text{F}_5$ at 544 and 555 nm was calculated (Figure 9b). For Yb^{3+} intensities at 966 and 1036 nm relative to 973 nm were calculated (Figure 9d,e,g,h for $\text{Yb}^{3+}/\lambda_{\text{ex}} = 780 \text{ nm}$ and $\text{Yb}^{3+}/\lambda_{\text{ex}} = 488 \text{ nm}$ emission, respectively).

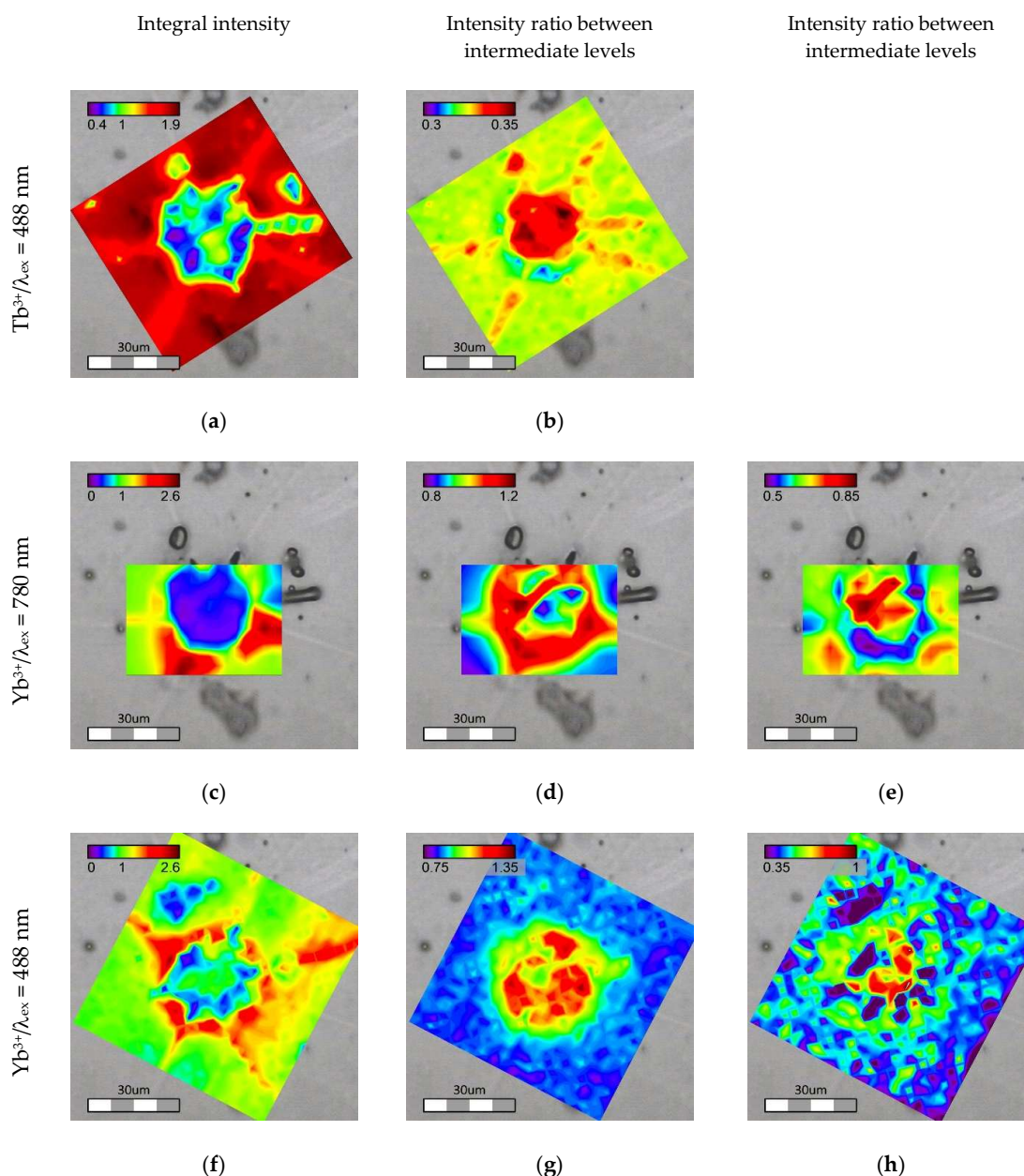


Figure 9. Results of detailed investigation of 1100/30 *Tb-Yb* sample using fluorescence microscopes: emission intensities of $\text{Tb}^{3+}/\lambda_{\text{ex}} = 488 \text{ nm}$ (a), $\text{Yb}^{3+}/\lambda_{\text{ex}} = 780 \text{ nm}$ (c) and $\text{Yb}^{3+}/\lambda_{\text{ex}} = 488 \text{ nm}$ (f); relative intensities of the emission peaks calculated as $I(555)/I(544)$ for Tb^{3+} (b), $I(966)/I(973)$ and $I(1036)/I(973)$ for Yb^{3+} excited under 780 nm (d and e, respectively) and under 488 nm (g and h, respectively). A rainbow palette was used for all the plots—violet and red colors correspond to the lowest and the highest value of the plotted value, respectively.

Under direct excitation, the integral minimum of luminescence intensity for both Tb^{3+} and Yb^{3+} coincides well with the t-ZrO₂ phase. At the same time, areas with maximum of Yb^{3+} luminescence were located close to ytterbium disilicate. The changes in the relative luminescence peak intensities are also strongly correlated with the crystals formed in the sample. The ratio between $^5\text{D}_4 \rightarrow ^7\text{F}_5$ subcomponents of Tb^{3+} emission has a pronounced maximum in the area of t-ZrO₂. Changes in Yb^{3+} luminescence were not so trivial. The relative intensity of the 966 nm peak increases close to the crystalline phases (both t-ZrO₂ and $\text{Yb}_2\text{Si}_2\text{O}_7$), but at the same time the maximum is observed around the t-ZrO₂ crystal rather than directly inside this area. The component at 1036 nm increases within the t-ZrO₂ phase and at the outer border of $\text{Yb}_2\text{Si}_2\text{O}_7$ whereas a minimum zone is observed around t-ZrO₂. Changes in the optical properties, in both intensity and the emission spectrum, suggest that REE are redistributed in different sites and phases present in the material, and the final optical characteristics depend on the local environment of the ions. Owing to a big ionic radii mismatch between the REE and Si, it is hardly possible that Tb and Yb enter cristobalite lattice, but they can substitute for Zr in crystalline ZrO₂. Decreases in the luminescence intensity observed for the t-ZrO₂ indicate that the concentration of the REE in the lattice is much less as compared to the amorphous phase. This assumption was confirmed with chemical analysis done locally with EDX. Only about 3 mol. % of Yb was still present in the tetragonal phase. Tb could not be detected because its concentration was below the detection limit.

The intensity of the Yb^{3+} luminescence mapping excited through the energy transfer from Tb^{3+} ($\lambda_{\text{ex}} = 488 \text{ nm}$) differs significantly from the directly excited one. The most intense emission was observed at the border of t-ZrO₂ and it did not coincide with the position of the Yb-disilicate phase (Figure 8). On the other hand, the changes in intensities at 966 and 1036 nm relative to 973 nm, determined in the same manner as for the directly excited Yb^{3+} luminescence ($\lambda_{\text{ex}} = 780 \text{ nm}$), are more pronounced in the t-ZrO₂ area (Figure 9g,h). One of the reasons for the less intense emission in t-ZrO₂ is lower concentration of the REE, which is probably partially compensated by higher luminescence efficiency in the crystal lattice as compared to the glassy phase.

Here it is important to understand the mechanism of the Tb \rightarrow Yb energy transfer, since quantum cutting implies the need for high doping concentration of the acceptor (here Yb^{3+}), which seems to be not the case for the formed t-ZrO₂. To better understand the mechanism of the energy transfer, emission intensity versus laser excitation power was measured in t-ZrO₂, at the t-ZrO₂/glass interface and in the glass area, far from the big crystalline inclusions. The dependence was found to be linear for the crystalline phase, and non-linear for both glass and interface areas (Figure 10).

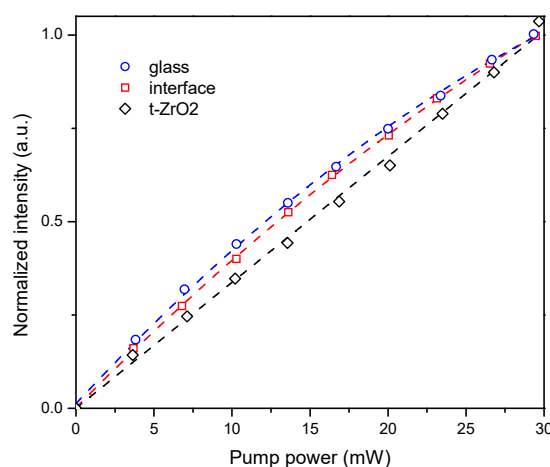


Figure 10. Intensity of Yb^{3+} luminescence versus incident laser power measured at different spots in 1100/30 Tb-Yb sample, $\lambda_{\text{ex}} = 488 \text{ nm}$, laser spot diameter during the experiment was $\sim 1.5 \mu\text{m}$.

According to the literature, non-linear dependence of luminescence intensity versus excitation power evidences second-order nonlinear quantum cutting process with energy transfer through a virtual energy level [32]. In turn, linear dependence in the case of t-ZrO₂ can be explained by the cooperative energy transfer process from ⁵D₄(Tb³⁺) to Yb³⁺ [32]. However, the existence of a unique energy transfer in the case of t-ZrO₂ is not irrefutable proof of the quantum cutting process. Typically, the Tb→Yb cooperative energy transfer is considered to be the most probable relaxation pathway from the ⁵D₄ excited state of the Tb³⁺ ion since the probability of the non-radiative multi-phonon relaxation needed to compensate the energy gap between the ⁵D₄ (Tb³⁺) and ³F_{5/2} (Yb³⁺) excited states, is small. In some materials the one-to-one energy transfer mechanism can dominate over the down-conversion process [33]. As was mentioned above, the concentration of the REE in the t-ZrO₂ crystalline phase decreased significantly when compared to the pristine glass, i.e., the possibility of finding an Yb–Yb pair in the nearest sphere of Tb³⁺ is much smaller. This typically results in a decreased rate in the cooperative energy transfer process. At the same time RE³⁺ substitution for Zr⁴⁺ in the t-ZrO₂ lattice requires charge compensation. The latter leads to the formation of oxygen vacancies, and as a consequence, different optical defect centers [34,35]. We suggest that these oxygen-related defects could serve as an additional energy sink capable of compensating the Tb–Yb energy gap, and one-to-one photon conversion cannot be completely excluded here.

Detailed comparison of the structural and luminescence properties in the 1100/30 Tb–Yb sample revealed that the changes in the optical properties are mostly determined by formation of different phases: the residual glass phase and three different crystalline phases. However, there is no evidence that Tb→Yb energy transfer in the crystals is more efficient when compared to the amorphous phase. The most intense emission of Yb³⁺, when excited through Tb³⁺ ion at 488 nm, was found at the interface between t-ZrO₂ crystal and the glass. This can be explained by the fact that the doping level of ZrO₂ with REE cannot be as high as for the glass and the excess Yb and Tb ions are displaced to the outer rim of the crystalline inclusions. This leads to the formation of a REE rich layer at the glass-crystal interface with higher energy transfer probability. Excessively high concentration of the REE can also lead to crystallization REE-containing phases, e.g., for 1100/30 Tb–Yb the presence of Yb₂Si₂O₇ was detected. The latter obviously excludes part of the Yb³⁺ ion from the energy transfer process since there is no donor Tb³⁺ ions in the near environment.

1100/30 Tb–Yb sample is the extreme point in the set of samples examined in this study: it had the highest crystallinity but became spatially inhomogeneous due to formation of large crystalline inclusions. However, we may assume that the phenomena happening under devitrification of the samples are the same, but less pronounced at lower time and temperature of the treatment. From this point of view, control of the crystalline phases and the size of the crystalline inclusion will play a crucial role in the final ETE, and this agrees with the experimental data obtained in the study. Moreover, many small crystals will have a higher surface as compared to a big crystal of the same volume, i.e., higher effective volume of the REE-rich material can be achieved, although too high a concentration of the REE could lead to self-quenching of the luminescence, decreasing the overall efficiency. This could explain why moderate heat treatment at 1000 °C results had higher Tb–Yb energy transfer efficiency as compared to the treatment at higher temperatures.

4. Conclusions

The results obtained in this study provide evidence that a sol-gel derived Tb–Yb doped 30ZrO₂–70SiO₂ system can be considered as a perspective for down-shifting applications and could be used as energy convertors in Si-solar cells. It was found that the efficiency of the Tb→Yb energy transfer significantly increased after devitrification of the amorphous media and the maximum value obtained in this study was 42%. We demonstrated that final structural properties of the material are determined by the crystallization process, which in turn, depends on time and temperature of the heat-treatment. During the devitrification, REE can serve as nucleation agents as well as form novel REE-bearing crystalline phases. After the heat treatment of Tb–Yb samples, formation of up to

3 different crystalline phases was observed within the samples that led to redistribution of the REE. This is considered to be one of the main influences on the final optical properties. The tetragonal ZrO_2 was found to be the dominant crystalline phase. It was found that even if Tb^{3+} and Yb^{3+} can enter into the lattice of the crystals, the most efficient Yb^{3+} emission, when excited through the energy transfer from Tb^{3+} , was observed at the interface between glassy and crystalline materials phases. This could be explained by the concentration of the REE at the outer rim of t-ZrO_2 , due to the inability of this phase to accept high amounts of Tb and Yb. The results of the present work can be used for future optimization of the Tb-Yb doped ZrO_2 - SiO_2 system as well as of different types of GC for potential spectral conversion applications.

Author Contributions: Investigation, M.I., V.A., M.R.C.; Writing-Original Draft Preparation, V.A.; Writing-Review & Editing, M.I. V.A., T.H., D.d.L.; Supervision, V.A., M.R.C., T.H., D.d.L.; Project Administration, T.H., D.d.L.

Acknowledgments: The authors are grateful to Jean Rene Duclere and Philippe Thomas from Laboratoire de Sciences des Procédés Ceramiques et de Traitements de Surface, University of Limoges (France) for fruitful discussions and helpful comments.

Conflicts of Interest: The authors declare no conflict of interest.

References

- Shockley, W.; Queisser, H.J. Detailed Balance Limit of Efficiency of p-n Junction Solar Cells. *J. Appl. Phys.* **1961**, *32*, 510–519. [\[CrossRef\]](#)
- Huang, X.; Han, S.; Huang, W.; Liu, X. Enhancing solar cell efficiency: The search for luminescent materials as spectral converters. *Chem. Soc. Rev.* **2013**, *42*, 173–201. [\[CrossRef\]](#) [\[PubMed\]](#)
- van der Ende, B.M.; Aarts, L.; Meijerink, A. Lanthanide ions as spectral converters for solar cells. *PCCP* **2009**, *11*, 11081–11095. [\[CrossRef\]](#) [\[PubMed\]](#)
- Vergeer, P.; Vlugt, T.J.H.; Kox, M.H.F.; den Hertog, M.I.; van der Eerden, J.P.J.M.; Meijerink, A. Quantum cutting by cooperative energy transfer in $\text{Yb}_x\text{Y}_{1-x}\text{PO}_4:\text{Tb}^{3+}$. *Phys. Rev. B* **2005**, *71*, 014119. [\[CrossRef\]](#)
- Bouajaj, A.; Belmokhtar, S.; Britel, M.R.; Armellini, C.; Boulard, B.; Belluomo, F.; Di Stefano, A.; Polizzi, S.; Lukowiak, A.; Ferrari, M.; et al. $\text{Tb}^{3+}/\text{Yb}^{3+}$ codoped silica-hafnia glass and glass-ceramic waveguides to improve the efficiency of photovoltaic solar cells. *Opt. Mater.* **2016**, *52*, 62–68. [\[CrossRef\]](#)
- An, Y.-T.; Labbé, C.; Cardin, J.; Morales, M.; Gourbilleau, F. Highly Efficient Infrared Quantum Cutting in Tb^{3+} – Yb^{3+} Codoped Silicon Oxynitride for Solar Cell Applications. *Adv. Opt. Mater.* **2013**, *1*, 855–862. [\[CrossRef\]](#)
- Zhang, Q.Y.; Yang, C.H.; Jiang, Z.H.; Ji, X.H. Concentration-dependent near-infrared quantum cutting in $\text{GdBO}_3:\text{Tb}^{3+}, \text{Yb}^{3+}$ nanophosphors. *Appl. Phys. Lett.* **2007**, *90*, 061914. [\[CrossRef\]](#)
- Zhang, Q.Y.; Yang, C.H.; Pan, Y.X. Cooperative quantum cutting in one-dimensional $(\text{Yb}_x\text{Gd}_{1-x})\text{Al}_3(\text{BO}_3)_4:\text{Tb}^{3+}$ nanorods. *Appl. Phys. Lett.* **2007**, *90*, 021107. [\[CrossRef\]](#)
- Nogami, M. Glass preparation of the ZrO_2 - SiO_2 system by the sol-gel process from metal alkoxides. *J. Non-Cryst. Solids* **1985**, *69*, 415–423. [\[CrossRef\]](#)
- Terra, I.A.A.; Borrero-González, L.J.; Carvalho, J.M.; Terrile, M.C.; Felinto, M.C.F.C.; Brito, H.F.; Nunes, L.A.O. Spectroscopic properties and quantum cutting in Tb^{3+} – Yb^{3+} co-doped ZrO_2 nanocrystals. *J. Appl. Phys.* **2013**, *113*, 073105. [\[CrossRef\]](#)
- Enrichi, F.; Armellini, C.; Belmokhtar, S.; Bouajaj, A.; Chiappini, A.; Ferrari, M.; Quandt, A.; Righini, G.C.; Vomiero, A.; Zur, L. Visible to NIR downconversion process in Tb^{3+} – Yb^{3+} codoped silica-hafnia glass and glass-ceramic sol-gel waveguides for solar cells. *J. Lumin.* **2018**, *193*, 44–50. [\[CrossRef\]](#)
- Bouchouicha, H.; Panczer, G.; de Ligny, D.; Guyot, Y.; Baesso, M.L.; Andrade, L.H.C.; Lima, S.M.; Ternane, R. Synthesis and luminescent properties of $\text{Eu}^{3+}/\text{Eu}^{2+}$ co-doped calcium aluminosilicate glass-ceramics. *J. Lumin.* **2016**, *169*, 528–533. [\[CrossRef\]](#)
- Kim, H.; McIntyre, P.C. Spinodal decomposition in amorphous metal-silicate thin films: Phase diagram analysis and interface effects on kinetics. *J. Appl. Phys.* **2002**, *92*, 5094–5102. [\[CrossRef\]](#)
- Gaudon, A.; Dager, A.; Lecomte, A.; Soulestin, B.; Guinebretière, R. Phase separation in sol-gel derived ZrO_2 - SiO_2 nanostructured materials. *J. Eur. Ceram. Soc.* **2005**, *25*, 283–286. [\[CrossRef\]](#)

15. Parfenenkov, V.N.; Grebenshchikov, R.G.; Toropov, N.A. Phase equilibriums in the hafnium dioxide–silicon dioxide system. *Dokl. Akad. Nauk SSSR* **1969**, *185*, 840–842.
16. Butterman, W.C.; Foster, W.R. Zircon stability and the $\text{ZrO}_2\text{-SiO}_2$ phase diagram. *Am. Mineral.* **1967**, *52*, 880–885.
17. Gaudon, A.; Lallet, F.; Boulle, A.; Lecomte, A.; Soulestin, B.; Guinebretière, R.; Dauger, A. From amorphous phase separations to nanostructured materials in sol–gel derived $\text{ZrO}_2\text{:Eu}^{3+}/\text{SiO}_2$ and ZnO/SiO_2 composites. *J. Non-Cryst. Solids* **2006**, *352*, 2152–2158. [[CrossRef](#)]
18. Veber, A.; Cicconi, M.R.; Reinfelder, H.; de Ligny, D. Combined Differential scanning calorimetry, Raman and Brillouin spectroscopies: A multiscale approach for materials investigation. *Anal. Chim. Acta* **2018**, *998*, 37–44. [[CrossRef](#)] [[PubMed](#)]
19. Lakowicz, J.R. *Principles of Fluorescence Spectroscopy*; Springer: New York, NY, USA, 2006; ISBN 978-0-387-31278-1.
20. Lee, S.W.; Condrate, R.A. The infrared and Raman spectra of $\text{ZrO}_2\text{-SiO}_2$ glasses prepared by a sol-gel process. *J. Mater. Sci.* **1988**, *23*, 2951–2959. [[CrossRef](#)]
21. Phillippi, C.M.; Mazdiyasi, K.S. Infrared and Raman Spectra of Zirconia Polymorphs. *J. Am. Ceram. Soc.* **1971**, *54*, 254–258. [[CrossRef](#)]
22. Keramidas, V.G.; White, W.B. Raman Scattering Study of the Crystallization and Phase Transformations of ZrO_2 . *J. Am. Ceram. Soc.* **1974**, *57*, 22–24. [[CrossRef](#)]
23. Feinberg, A.; Perry, C.H. Structural disorder and phase transitions in $\text{ZrO}_2\text{-Y}_2\text{O}_3$ system. *J. Phys. Chem. Solids* **1981**, *42*, 513–518. [[CrossRef](#)]
24. Cai, J.; Raptis, Y.S.; Anastassakis, E. Stabilized cubic zirconia: A Raman study under uniaxial stress. *Appl. Phys. Lett.* **1993**, *62*, 2781–2783. [[CrossRef](#)]
25. Li, P.; Chen, I.-W.; Penner-Hahn, J.E. Effect of Dopants on Zirconia Stabilization-An X-ray Absorption Study: I, Trivalent Dopants. *J. Am. Ceram. Soc.* **1994**, *77*, 118–128. [[CrossRef](#)]
26. Aguilar, D.H.; Torres-Gonzalez, L.C.; Torres-Martinez, L.M.; Lopez, T.; Quintana, P. A Study of the Crystallization of ZrO_2 in the Sol–Gel System: $\text{ZrO}_2\text{-SiO}_2$. *J. Solid State Chem.* **2001**, *158*, 349–357. [[CrossRef](#)]
27. Masahiro, Y. Phase stability of zirconia. *Am. Ceram. Soc. Bull.* **1988**, *67*, 1950–1955.
28. Ito, J.; Johnson, H. Synthesis and study of yttrialite. *Am. Mineral.* **1968**, *53*, 1940–1952.
29. Tian, Z.; Zheng, L.; Li, Z.; Li, J.; Wang, J. Exploration of the low thermal conductivities of $\gamma\text{-Y}_2\text{Si}_2\text{O}_7$, $\beta\text{-Y}_2\text{Si}_2\text{O}_7$, $\beta\text{-Yb}_2\text{Si}_2\text{O}_7$, and $\beta\text{-Lu}_2\text{Si}_2\text{O}_7$ as novel environmental barrier coating candidates. *J. Eur. Ceram. Soc.* **2016**, *36*, 2813–2823. [[CrossRef](#)]
30. Kaindl, R.; Többsen, D.M.; Kahlenberg, V. DFT-aided interpretation of the Raman spectra of the polymorphic forms of $\text{Y}_2\text{Si}_2\text{O}_7$. *J. Raman Spectrosc.* **2011**, *42*, 78–85. [[CrossRef](#)]
31. Mysen, B.O.; Virgo, D.; Scarfe, C.M. Relations between the anionic structure and viscosity of silicate melts—A Raman spectroscopic study. *Am. Mineral.* **1980**, *65*, 690–710.
32. Duan, Q.; Qin, F.; Zhang, Z.; Cao, W. Quantum cutting mechanism in $\text{NaYF}_4\text{:Tb}^{3+}, \text{Yb}^{3+}$. *Opt. Lett.* **2012**, *37*, 521. [[CrossRef](#)] [[PubMed](#)]
33. Hu, J.; Zhang, Y.; Xia, H.; Ye, H.; Chen, B.; Zhu, Y. NIR Downconversion and Energy Transfer Mechanisms in $\text{Tb}^{3+}/\text{Yb}^{3+}$ Codoped $\text{Na}_5\text{Lu}_9\text{F}_{32}$ Single Crystals. *Inorg. Chem.* **2018**, *57*, 7792–7796. [[CrossRef](#)] [[PubMed](#)]
34. de Sousa, W.S.C.; Melo, D.M.A.; da Silva, J.E.C.; Nasar, R.S.; Nasar, M.C.; Varela, J.A. Photoluminescence in ZrO_2 doped with Y and La. *Cerâmica* **2007**, *53*, 99–103. [[CrossRef](#)]
35. Smits, K.; Olsteins, D.; Zolotarjovs, A.; Laganovska, K.; Millers, D.; Ignatans, R.; Grabis, J. Doped zirconia phase and luminescence dependence on the nature of charge compensation. *Sci. Rep.* **2017**, *7*. [[CrossRef](#)] [[PubMed](#)]

